Research Article | Vol. 31, No. 24 / 20 Nov 2023 / Optics Express 40450
Optics EXPRESS

Pixel-wise beam-hardening correction for dark-field signal in X-ray dual-phase grating interferometry

RUIZHI TANG,[1,2,*] CAORI ORGANISTA,[1,2,3,4] LUCIA ROMANO,[3,4] LUC VAN HOOREBEKE,[1,2] MARCO STAMPANONI,[3,4] JAN AELTERMAN,[1,2,5] AND MATTHIEU N. BOONE[1,2]

[1]*Ghent University Centre for X-Ray Tomography (UGCT), Proeftuinstraat 86/N12, 9000 Ghent, Belgium*
[2]*Radiation Physics Research Group, Department of Physics and Astronomy, Ghent University, Proeftuinstraat 86, 9000 Ghent, Belgium*
[3]*Swiss Light Source, Paul Scherrer Institute, 5232 Villigen, Switzerland*
[4]*Institute for Biomedical Engineering, University and ETH Zurich, 8092 Zurich, Switzerland*
[5]*IPI-TELIN-IMEC, Ghent University, Ghent, Belgium*
[*]*Ruizhi.Tang@UGent.be*

Abstract: The dark-field signal provided by X-ray grating interferometry is an invaluable tool for providing structural information beyond the direct spatial resolution and their variations on a macroscopic scale. However, when using a polychromatic source, the beam-hardening effect in the dark-field signal makes the quantitative sub-resolution structural information inaccessible. Especially, the beam-hardening effect in dual-phase grating interferometry varies with spatial location, inter-grating distance, and diffraction order. In this work, we propose a beam-hardening correction algorithm, taking into account all these factors. The accuracy and robustness of the algorithm are then validated by experimental results. This work contributes a necessary step toward accessing small-angle scattering structural information in dual-phase grating interferometry.

1. Introduction

X-ray Talbot grating interferometry (XT-GI) has made great progress in the past 20 years and has proven its huge potential in both medical imaging and material science [1–10]. XT-GI is capable of providing additional complementary information, notably differential phase contrast and dark-field signal, in addition to the attenuation contrast that can be obtained through conventional X-ray radiography. Furthermore, XT-GI is able to provide a large field of view and maintain a compact set-up, while remaining compatible with broadband laboratory sources. The principle of XT-GI is based on the Talbot effect [11] to generate a periodic interference pattern. By quantitatively analyzing how the interference pattern is changed by a sample, three complementary signals of the sample can be retrieved. In traditional Talbot grating interferometry, a phase grating is used to diffract the incoming beam and an interference pattern is formed downstream at the fractional Talbot distances [1,3]. Normally, since the period of the interference pattern is generally too small to be directly resolved by a detector, an absorption (or analyzer) grating with the same period and orientation as the interference pattern is placed immediately in front of the detector. Then, a phase-stepping approach is implemented [3]. By scanning one of the gratings along the transverse direction, the intensity oscillation of the interference pattern is recorded by each pixel as a phase stepping curve, so that the detector resolution is decoupled from the fringe period. For the X-rays sources without enough transverse spatial coherence to generate a high-contrast interference pattern, a source mask is placed close to the X-ray source to fulfill the coherence requirement [4].

#499397 https://doi.org/10.1364/OE.499397
Journal © 2023 Received 30 Jun 2023; revised 14 Sep 2023; accepted 18 Sep 2023; published 15 Nov 2023

Optics EXPRESS

The phase stepping curve in XT-GI can be approximated by the Fourier series up to the first order [3,6]:

$$I_{\text{Talbot}}(x_g) = a_0 + a_1 \cdot \cos\left(2\pi \frac{x_g}{p_g} + \phi_1\right), \tag{1}$$

where x_g and p_g are the transverse position and pitch size of the stepped grating respectively, a_0 is the averaged intensity, a_1 and ϕ_1 are the corresponding amplitude and phase for the 1st harmonics, respectively. With a sample placed in the beam, the phase stepping curve is altered since the sample's structural information is imprinted onto the wavefront. The reduction of a_0 is related to the line integral of the attenuation coefficient based on the Beer-Lambert law. The shift of ϕ_1 is related to the transverse gradient of the projected phase shift [1,3]. Both retrieved absorption and differential phase contrast result from the smooth features of the sample within the resolution of the system. Meanwhile, the unresolvable features cause a reduction of visibility and generate the so-called dark-field signal, where visibility is defined as the ratio between the amplitude and the averaged intensity: $V = a_1/a_0$[6].

Since this visibility decaying follows the same exponential relation with the sample thickness as in the attenuation modality [12,13], in analogy to the attenuation coefficient, the dark-field extinction coefficient u_d is used to quantify this visibility decrease. The specific expression for u_d has been derived from both wave calculations [14,15] and scattering theory [16,17]. Here, we adopted the formula derived by Strobl [16], as it clearly indicates the relation between the dark-field extinction coefficient and quantitative small-angle scattering (SAS) information:

$$u_d = \Sigma(1 - G(\xi)), \tag{2}$$

where Σ represents the macroscopic scattering cross section and the correlation function $G(\xi)$ is the projection of the auto-correlation function of unresolvable features at the correlation length ξ[14–16,18]. The correlation length is a characteristic length that is a function of the geometry of the set-up, sample position, and x-ray wavelength. Given the fact that the correlation function is related to the projected scattering function on the transverse axis by a cosine Fourier transform [16,19], quantitative sub-resolution structural information is then accessible from the relation between dark-field signal and correlation length. This means that dark-field imaging has the unique ability to simultaneously combine macroscopic spatial resolution and SAS structural information by scanning the correlation length.

However, XT-GI still has some disadvantages. Firstly, since the analyzer grating absorbs nearly half of the information-carrying photons behind the sample, this significantly reduces the dose efficiency. Secondly, it is still a challenge to fabricate absorption gratings with high aspect ratios and large areas [20]. Furthermore, tuning the correlation length in XT-GI is normally related to changes in the sample's magnification when a cone beam geometry is considered [15–17,21–23]. This hinders accessing sub-resolution structural information for each pixel from the dark-field signal. Although another alternative to change the correlation length is by adjusting the photon energy [24], this is far from trivial when using a polychromatic source. In order to solve these problems, dual-phase grating interferometry (DPGI) has recently been proposed [25,26]. Unlike XT-GI forming a periodic pattern based on the Talbot effect, in DPGI a Moiré fringe generated by two phase gratings with slightly different magnifications can be directly resolved [27,28]. Therefore, using an analyzer grating is not necessary. Moreover, tuning the correlation length in DPGI can be achieved by adjusting the inter-grating distance R_g (see Fig. 1) without influencing the sample's magnification [26,29]. Similar to XT-GI, a source mask is added in DPGI to fulfil the generalized Lau condition when the X-ray sources cannot provide enough spatial coherence [30–32].

In principle, both XT-GI and DPGI can provide three independent contrasts. However, when a polychromatic source is used, these contrasts begin to couple with each other. Since photon energy affects both the phase-shift values of gratings and wave propagation, the resulting interference

Optics EXPRESS

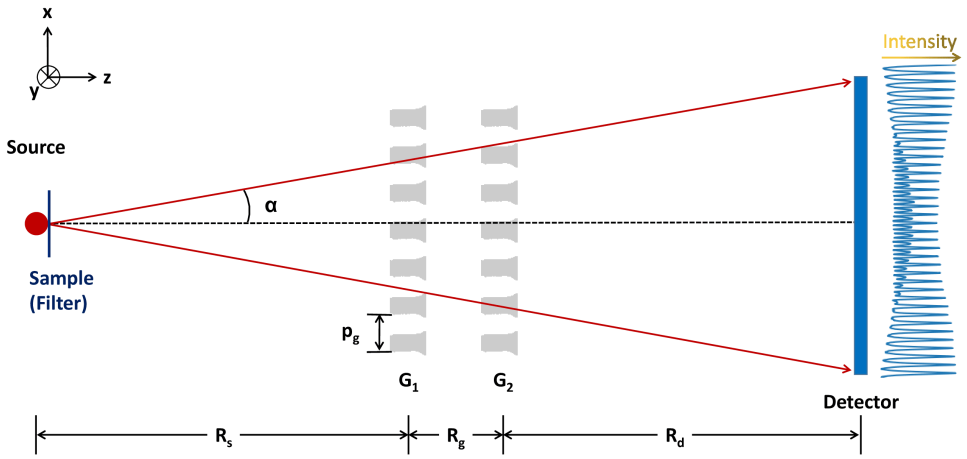

Fig. 1. Schematic of dual-phase grating interferometry. The X-rays are generated by a micro-focus tube, propagate through two adjacent phase gratings, and are recorded by an integrating detector. A typical interference pattern on the x-axis is plotted behind the detector, indicating that the fringe is closely related to the divergence angle. The grating shape is inspired by Fig. 7, to represent the deviations from a perfect rectangular shape. The position of the sample is represented by a blue solid line, attached to the exit window of the X-ray tube.

pattern changes with photon energy, leading to a spectral dependence in its visibility [33,34]. Meanwhile, the fringes detected by an integrating detector are the result of the incoherent summation of the interference pattern formed by each photon energy, with the weights of each energy given by the spectrum [35]. Due to the unequal attenuation for each photon energy as it passes through the sample, the spectrum behind the sample is reshaped. Consequently, the attenuation affects the extracted visibility and phase information obtained from the polychromatic interference pattern, resulting in the so-called beam-hardening effects in differential phase contrast [33,36–39] and dark-field signal [40–43]. The beam-hardening effect will introduce an extra dark-field signal besides the small-angle scattering. However, this effect behaves differently between XT-GI and DPGI when scanning the correlation length. In XT-GI, since the correlation length is normally tuned by moving the sample along the beam axis without changing the geometry of the set-up, the spectral properties of the set-up are kept the same, therefore, the dark-field signal attributed to the attenuation is constant among all correlation lengths. Conversely, in DPGI, the correlation length is adjusted by changing the inter-grating distance, which impacts the spectral properties [27,34,43,44]. This leads to a varying effect on the attenuation-based dark-field signal in response to the correlation length, making it impossible to quantitatively analyze the sub-resolution structural information.

Pandeshwar et al. proposed an analytical model based on wave propagation theory to address the issue of beam-hardening effect in DPGI [43]. Their model quantitatively analyzes the impact of varying beam-hardening effects on the dark-field signal across different correlation lengths and provides a solution to retrieve the dark-field signal only related to the small-angle scattering. However, this model has several limitations based on our recent findings [44]. Firstly, given the fact that the phase gratings used have large aspect ratios, the transmission profile of the grating changes rapidly with the incident angle in a cone beam geometry. As a result, the interference patterns in DPGI are strongly influenced by the divergence angle α. As depicted in Fig. 1, the amplitude of the interference pattern changes with the divergence angle, and intermediate peaks are presented in the middle of the pattern. The variations in the transmission profile

Optics EXPRESS

also imply a spatially-varying spectral property, which consequently causes a beam-hardening effect in the dark-field signal that is also dependent on the divergence angle. Nevertheless, the analytical model solely accounts for the scenario of a normal incident. The second limitation of the analytical model is that it assumes the grating bars to be rectangular and to only contain phase modulation, neglecting any absorption effects. To be more precise, the real grating bars exhibit deviations from the perfect rectangular shape and are not completely devoid of absorption properties. Thirdly, the analytical model only considers the first diffraction order, while the higher diffraction orders are not negligible in DPGI [28]. As illustrated in Fig. 1, the second-order diffraction pattern is represented by the smaller secondary peaks. Therefore, in this work, we set out to develop a beam-hardening correction algorithm that accounts for the spatially-dependent spectral properties, as well as a realistic grating shape and higher diffraction orders. Moreover, the accuracy and robustness of the algorithm are validated by applying the beam-hardening correction to a variety of samples.

2. Method

Before presenting the algorithm for beam-hardening correction, a brief background of the set-up is described. As shown in Fig. 1, R_s is source-to-G_1 distance, R_d is G_2-to-detector distance, and R_g is inter-grating distance, where $R_g \ll R_s \approx R_d$. Two gratings are assumed to be identical with period p_g which is much smaller than the pixel size of the detector. To fine-tune the correlation length, the inter-grating distance R_g is adjusted by moving G_2 a distance on the same order of magnitude as R_g along the z-axis, while keeping G_1 fixed. Although the detector can directly resolve the fringes, the phase stepping approach is used to record the local intensity profiles in each pixel, by stepping G_1 for one period along the x-axis.

According to the derivations given by Yan et al. [27,28] and Miao et al. [25], the interference patterns produced in DPGI are achromatic, meanwhile, the higher harmonic signals are not negligible. Moreover, the interference patterns are also influenced by the spatial location and inter-grating distance [44]. Firstly, we consider a monochromatic situation in which a wavefront with an intensity of I_0 uniformly illuminates G_1. Incorporating all these factors, we formulate the phase stepping curve (reference scan) as:

$$I_{\mathrm{ref}}^{(i,j,R_g)}(x_g, E) = \frac{I_0}{M}\left[a_0^{(i)}(E) + \sum_{l=1}^{\infty} a_l^{(i,R_g)}(E)\cdot\cos\left(2\pi l\left(\frac{x_g}{p_g} + \phi^{(i,R_g)}\right)\right)\right]. \tag{3}$$

The pixel indices, i and j, account for the spatial location, and R_g is the inter-grating distance. The phase stepping curve is a function of the transverse position x_g of the stepped grating (G_1) and photon energy E. To account for the cone beam geometry, the incident intensity I_0 is reduced according to a magnification factor: $M = \frac{R_s}{R_s+R_g+R_d}$. The intensity oscillation is described by a summation of different harmonics, with the diffraction order represented by l. As both gratings are aligned along the y-axis, the mean value a_0, the amplitude a_l and the reference phase ϕ are uniform along the y-axis, meaning they are independent of the index j. The mean value a_0 is related to the attenuation of two gratings, and it will be shown later that a_0 can be considered as constant among the inter-grating distances. Moreover, the amplitude a_l is related to the transmission function of the gratings, the degree of coherence of the source, the geometry of the set-up, and the response function of the detector [27]. Therefore, both a_0 and a_l are dependent on the photon energy. Similar to the definition of the visibility in XT-GI, the visibility coefficient in DPGI is defined as $V_l(E) = \frac{a_l(E)}{a_0(E)}$. Using this definition, we can rewrite Eq. (3) as:

$$I_{\mathrm{ref}}^{(i,j,R_g)}(x_g, E) = \frac{I_0}{M}\left[a_0^{(i)}(E) + \sum_{l=1}^{\infty} a_0^{(i)}(E)\cdot V_l^{(i,R_g)}(E)\cdot\cos\left(2\pi l\left(\frac{x_g}{p_g} + \phi^{(i,R_g)}\right)\right)\right]. \tag{4}$$

Optics EXPRESS

When a sample is introduced to a beam, the intensity of the fringes as well as the visibility coefficient decreases. The degree of reduction is determined by the line integral of the attenuation coefficient and the dark-field extinction coefficient, respectively. At this point, the differential phase contrast resulting from the sample has not been taken into account. However, its effect will be discussed in Section 4. Therefore, the phase stepping curve with a sample is given as:

$$I_{\mathrm{s}}^{(i,j,R_{\mathrm{g}})}(x_{\mathrm{g}},E)=\frac{I_0}{M}\cdot T^{(i,j)}(E)\cdot \left[a_0^{(i)}(E)+\sum_{l=1}^{\infty}a_0^{(i)}(E)\cdot V_l^{(i,R_{\mathrm{g}})}(E)\cdot D_l^{(i,j,R_{\mathrm{g}})}(E)\cdot\cos\left(2\pi l\left(\frac{x_{\mathrm{g}}}{p_{\mathrm{g}}}+\phi^{(i,R_{\mathrm{g}})}\right)\right)\right], \tag{5}$$

with

$$T^{(i,j)}(E)=\exp\left[-\int\mu^{(i,j)}(E,z)dz\right], \tag{6}$$

$$D_l^{(i,j,R_{\mathrm{g}})}(E)=\exp\left[-\int\mu_{\mathrm{d}}^{(i,j,R_{\mathrm{g}},l)}(E,z)dz\right]. \tag{7}$$

The attenuation function $T(E)$, as presented in Eq. (6), follows the Beer-Lambert law, describing the relationship between the attenuation of intensity and the attenuation coefficient μ. Similarly, the reduction function of the visibility coefficient $D_l(E)$ in Eq. (7) follows the same exponential relation to the dark-field extinction coefficient μ_{d}. Based on Eq. (2), the dark-field extinction coefficient μ_{d} is related to the macroscopic scattering function and correlation length. When the sample is located upstream of G_1, the correlation length is defined as [29]:

$$\xi_{\mathrm{DPGI}}=-l\frac{\lambda L_{\mathrm{s}}}{p_{\mathrm{g}}}\cdot\frac{R_{\mathrm{g}}}{R_{\mathrm{s}}+R_{\mathrm{g}}+R_{\mathrm{d}}}, \tag{8}$$

where λ represents the wavelength and L_{s} is the source-sample distance. Eq. (8) demonstrates how the correlation length is adjusted by R_{g}, and indicates that the correlation length is dependent on the photon energy E and the diffraction order l. Given that the macroscopic scattering function is also energy-dependent, therefore, the dark-field extinction coefficient varies with the inter-grating distance, the diffraction order, and the photon energy.

When a polychromatic source is used, due to linearity, one may formulate the detected phase stepping curve as a summation of the phase stepping curve for each photon energy, with the weights determined by the spectral distribution $S_0(E)$, given by:

$$\hat{I}(x_{\mathrm{g}})=\sum_E S_0(E)I(E), \tag{9}$$

where the hat is used to represent the quantities estimated in the model for the polychromatic source. The effective intensity spectrum $S_0(E)$ comprises the source spectrum, the quantum efficiency, and the dose deposition of the detector. Then, the effective spectrum is further modified by several absorbers in the beam, which uniformly attenuates the wavefront without significant diffraction or refraction effects, such as air and grating substrate. Combining Eq. (4) and (9), the phase stepping curve of the reference scan is expressed in the polychromatic forms as:

$$\hat{I}_{\mathrm{ref}}^{(i,j,R_{\mathrm{g}})}(x_{\mathrm{g}})=\hat{a}_{0,\mathrm{ref}}^{(i,j)}+\sum_{l=1}^{\infty}\hat{a}_{l,\mathrm{ref}}^{(i,j)}\cdot\cos\left(2\pi l\left(\frac{x_{\mathrm{g}}}{p_{\mathrm{g}}}+\phi^{(i,R_{\mathrm{g}})}\right)\right), \tag{10}$$

with

$$\hat{a}_{0,\mathrm{ref}}^{(i,j)}=\frac{I_0}{M}\sum_E S_0(E)\cdot a_0^{(i)}(E), \tag{11}$$

Optics EXPRESS

$$\hat{a}_{l,\mathrm{ref}}^{(i,j)} = \frac{I_0}{M} \sum_E S_0(E) \cdot a_0^{(i)}(E) \cdot V_l^{(i,R_\mathrm{g})}(E). \tag{12}$$

Similarly, the sample scan is formulated as:

$$\hat{I}_\mathrm{s}^{(i,j,R_\mathrm{g})}(x_\mathrm{g}) = \hat{a}_{0,\mathrm{s}}^{(i,j)} + \sum_{l=1}^{\infty} \hat{a}_{l,\mathrm{s}}^{(i,j)} \cdot \cos\left(2\pi l \left(\frac{x_\mathrm{g}}{p_\mathrm{g}} + \phi^{(i,R_\mathrm{g})}\right)\right). \tag{13}$$

with

$$\hat{a}_{0,\mathrm{s}}^{(i,j)} = \frac{I_0}{M} \sum_E S_0(E) \cdot a_0^{(i)}(E) \cdot T^{(i,j)}(E), \tag{14}$$

$$\hat{a}_{l,\mathrm{s}}^{(i,j)} = \frac{I_0}{M} \sum_E S_0(E) \cdot a_0^{(i)}(E) \cdot V_l^{(i,R_\mathrm{g})}(E) \cdot T^{(i,j)}(E) \cdot D_l^{(i,j,R_\mathrm{g})}(E). \tag{15}$$

By applying the Fourier transform on the phase stepping curves for the polychromatic situation, the pixel-wise mean intensity $\hat{a}_0^{(i,j)}$ and amplitude $\hat{a}_l^{(i,j,R_\mathrm{g})}$ are retrieved from the corresponding Fourier coefficients for both reference and sample scans. Consequently, the visibility coefficient for the polychromatic source is calculated as $\hat{V}_l^{(i,j,R_\mathrm{g})} = \frac{\hat{a}_l^{(i,j,R_\mathrm{g})}}{\hat{a}_0^{(i,j)}}$. The spectral-averaged attenuation contrast is retrieved from the ratio of the mean intensity between the sample and the reference:

$$\begin{aligned} \hat{T}^{(i,j)} &= \frac{\hat{a}_{0,\mathrm{s}}^{(i,j)}}{\hat{a}_{0,\mathrm{ref}}^{(i,j)}} \\ &= \frac{\sum_E S_0 \cdot a_0^{(i)} \cdot T^{(i,j)}}{\sum_E S_0 \cdot a_0^{(i)}}. \end{aligned} \tag{16}$$

For the sake of simplicity, the energy dependencies for S_0, $a_0^{(i)}$, and $T^{(i,j)}$ are not explicitly stated. The extracted attenuation contrast in DPGI is identical to the results measured in conventional radiography, except that the effective spectrum is hardened by two gratings with a factor $a_0^{(i)}(E)$. In other words, the retrieved attenuation contrast is the weighted average of the attenuation function $T^{(i,j)}(E)$, as given in Eq. (6), with the weights related to $S_0(E) \cdot a_0^{(i)}(E)$. Similarly, the ratio of the visibility coefficient between the sample and the reference in the polychromatic source is formulated as:

$$\begin{aligned} \hat{D}_l^{(i,j,R_\mathrm{g})} &= \frac{\hat{V}_{l,\mathrm{s}}^{(i,j,R_\mathrm{g})}}{\hat{V}_{l,\mathrm{ref}}^{(i,j,R_\mathrm{g})}} \\ &= \frac{\sum_E S_0 \cdot a_0^{(i)} \cdot V_l^{(i,R_\mathrm{g})} \cdot T^{(i,j)} \cdot D_l^{(i,j,R_\mathrm{g})}}{\sum_E S_0 \cdot a_0^{(i)} \cdot T^{(i,j)}} \cdot \frac{\sum_E \cdot S_0 \cdot a_0^{(i)}}{\sum_E \cdot S_0 \cdot a_0^{(i)} \cdot V_l^{(i,R_\mathrm{g})}}. \end{aligned} \tag{17}$$

Here, we adopt a similar idea as presented in [41,43], which involves separating the change of the visibility coefficient into two components: SAS and attenuation, respectively. By introducing a factor $\sum_E S_0 \cdot a_0^{(i)} \cdot V_l^{(i,R_\mathrm{g})} \cdot T^{(i,j)}$ into Eq. (17), the change of the visibility coefficient can be

Optics EXPRESS

formulated as:

$$\hat{D}_l^{(i,j,R_g)} = \hat{D}_{l,\mathrm{SAS}}^{(i,j,R_g)} \cdot \hat{D}_{l,\mathrm{att}}^{(i,j,R_g)}, \tag{18}$$

with

$$\hat{D}_{l,\mathrm{SAS}}^{(i,j,R_g)} = \frac{\sum_E S_0 \cdot a_0^{(i)} \cdot V_l^{(i,R_g)} \cdot T^{(i,j)} \cdot D_l^{(i,j,R_g)}}{\sum_E S_0 \cdot a_0^{(i)} \cdot V_l^{(i,R_g)} \cdot T^{(i,j)}}, \tag{19}$$

$$\hat{D}_{l,\mathrm{att}}^{(i,j,R_g)} = \frac{\sum_E S_0 \cdot a_0^{(i)} \cdot V_l^{(i,R_g)} \cdot T^{(i,j)}}{\sum_E \cdot S_0 \cdot a_0^{(i)} \cdot V_l^{(i,R_g)}} \cdot \frac{\sum_E \cdot S_0 \cdot a_0^{(i)}}{\sum_E S_0 \cdot a_0^{(i)} \cdot T^{(i,j)}}. \tag{20}$$

In analogy to Eq. (16), the scattering-based visibility coefficient reduction $\hat{D}_{l,\mathrm{SAS}}^{(i,j,R_g)}$ is the weighted average of $D_l^{(i,j,R_g)}(E)$, as given in Eq. (7), with the weights determined by $S_0(E) \cdot a_0^{(i)}(E) \cdot V_l^{(i,R_g)}(E) \cdot T^{(i,j)}(E)$. Thus, this part of visibility coefficient reduction is solely attributed to the SAS signals, while the other part, $\hat{D}_{l,\mathrm{att}}^{(i,j,R_g)}$, results from attenuation. In the case of a broadband spectrum, the attenuation function $T^{(i,j)}(E)$ cannot be treated as a constant. When the attenuation is not negligible, $\hat{D}_{l,\mathrm{att}}^{(i,j,R_g)}$ could deviate from 1, and this deviation causes an additional impact on the visibility reduction beyond SAS. This leads to the beam-hardening effect in the dark-field signal. Moreover, the magnitude of the beam-hardening effect varies with the spatial position, inter-grating distance, and diffraction order. As a result, quantitative sub-resolution structural information is not accessible from the relation between the dark-field signal and correlation length. Nevertheless, based on the explicit expression of $\hat{D}_{l,\mathrm{att}}^{(i,j,R_g)}$, we can eliminate the beam-hardening effect and relate dark-field signal only to the SAS signals. This can be achieved provided that the spectral properties of the setup, which include $S_0(E)$, $a_0^{(i)}(E)$, and $V_l^{(i,R_g)}(E)$, as well as the attenuation function $T^{(i,j)}(E)$, are accurately estimated.

3. Experiment and results

To validate the beam-hardening correction algorithm, firstly, we implemented the phase scanning technique to extract the pixel-wise visibility coefficients at a number of inter-grating distances as the reference scans. Then, under the same geometrical settings, we conducted multiple measurements by introducing different samples one at a time into the beam. The samples were chosen to act as filters that only uniformly attenuate the wavefront and produce negligible small-angle scattering signals. This was intentional to make the visibility coefficient change originate only from the beam-hardening effect (attenuation rather than SAS). Finally, we implemented the previously described algorithm to correct the experimental results and evaluated the success of the beam-hardening removal in the dark-field signal.

3.1. Experimental settings

The experiments were conducted by using a transmission-type microfocus X-ray tube (FXT-160.51, FEINFOCUS GmbH, Germany), using a 1 µm tungsten-coated CVD diamond transmission anode. The tube was operated in microfocus mode at 40 kV and 200 µA. The JIMA pattern measurement indicated that the full width at half maximum (FWHM) of the source size was around 5 µm. The fringes were resolved by an sCMOS camera (Gsense, PHOTONIC SCIENCE, UK) coupled to a 100 µm CsI:TI scintillator. The detector featured an active input area of $67 \times 67\mathrm{mm}^2$ and an effective pixel size of $16.4 \times 16.4\mathrm{um}^2$. Two identical phase gratings were etched in 250 µ thick silicon substrates at the same depth (28 µ), as previously reported [34]. The grating pattern has been realized by displacement Talbot lithography with a period of 1 µ and a duty cycle of 0.5, the etching depth of 28 µ was designed to introduce a π phase shift at the X-ray energy of 22 keV. The deep reactive ion etching [20] of the two phase gratings has been

Optics EXPRESS

performed in two consecutive runs to guarantee the same plasma conditions for the best replica of the structural features in the two identical gratings. The total length of the set-up between the source and detector was kept at 1003 mm, and G_1 was placed 503 mm away from the X-ray tube. The second phase grating, G_2, was positioned downstream of G_1, and its position was adjusted by a linear stage (CLS-5282-L, SmarAct GmbH, Germany) to tune the inter-grating distance from 2.13 mm to 11.13 mm in increments of 1 mm. During the phase stepping process, G_1 was stepped in the transverse direction for a total of 8 times over one period, controlled by a linear positioner (CLS-5252-L, SmarAct GmbH, Germany). For each step, the interference pattern was recorded with an exposure time of 15 s. The samples (or filters) were attached to the exit window of the X-ray tube (see Fig. 1), to minimize the impact of Compton scattering on visibility [42]. This is not the sample position in typical DPGI measurements, yet we are only interested in the photon absorption of the filters, which is not influenced by the position

3.2. Spectral properties modelling

One necessary step to implement our beam-hardening correction algorithm is to accurately estimate the spectral properties of the set-up. This involves modeling the source spectrum by using a Monte Carlo simulator [45] and then attenuating it by several uniform absorbers, including air (1000 mm), a carbon fibre input window of the detector (1 mm), silicon substrates of two gratings (2×0.222mm), and a diamond window at the exit surface of X-ray tube (0.26 mm). After accounting for the quantum efficiency and the dose deposition of the scintillator, we obtain the effective spectrum $S_0(E)$, which is plotted in Fig. 2.

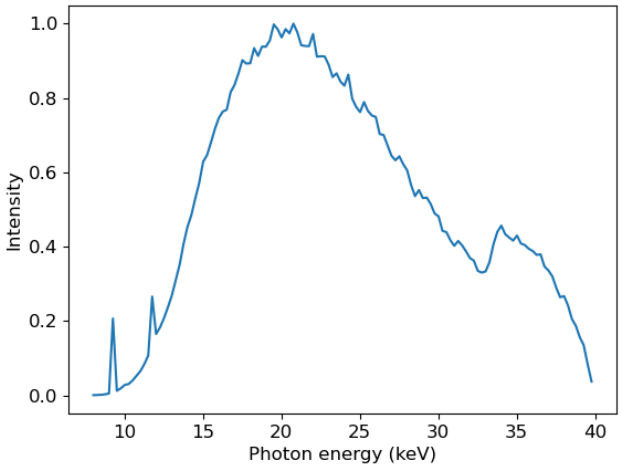

Fig. 2. Effective spectrum modeled in the simulation for tungsten target at 40 kV. The energy range is from 8 keV to 40 keV, with a sampling rate of 4 keV^{-1}.

Our next objective is to characterize how the mean-value spectrum $a_0(E)$ and visibility coefficient spectrum $V_l(E)$ change with respect to the transverse pixel index i and inter-grating distance R_g. To incorporate complicated features into the model such as spatially dependent transmission profiles of the gratings, a realistic shape of grating bars, as well as the measured detector response function (unsharpness), we implement a simulator based on the Fresnel wave propagation to extract the pixel-wise spectral properties. The algorithm of the simulator has been illustrated and validated in [44]. For a brief overview, the process involves propagating a wave field from a monochromatic extended source through two gratings and arriving at the detector plane. Then, the resulting interference pattern is simulated by including a realistic detector response function. The phase stepping process is also simulated by transversely moving G_1 a

Optics EXPRESS

total of 8 steps over one period. Finally, by applying Fourier transform on the phase stepping curve, the mean value a_0 and visibility coefficient V_l are retrieved from the Fourier coefficients for each pixel. By iterating through the energy range of the spectrum, the spectral properties are modeled. The simulator's settings have been maintained consistent with our corresponding experiment. More details of the simulation are illustrated in Section 6.

The spectral properties are compared in Fig. 3 for the two different inter-grating distances, shown in the left and right columns, respectively. Without losing generality, the results only for the first diffraction order are presented. Both Fig. 3 (a) and (b) show the spatial and energy dependencies of the 1st-order visibility coefficient V_1, where the x-axis is the divergence angle, the y-axis is the photon energy and the grey value represents the magnitude of the visibility coefficient. For a more intuitive illustration, the pixel index i is converted into the divergence angle based on the set-up geometry (see Fig. 1). The range of divergence angles between $-1.09°$ and $1.09°$ corresponds to a field of view of 38 mm along the x-axis. It is clearly indicated that the visibility coefficient spectrum $V_1(E)$, along the axis of photon energy, undergoes a significant change as the divergence angle varies. Additionally, the symmetry around zero degrees is also observed in $V_1(E)$. As previously discussed, this spatial dependence is a result of the angular-dependent transmission profile of the gratings. Moreover, there is a noticeable impact on the visibility coefficient when the inter-grating distance is changed, as can be observed by comparing Fig. 3 (a) and (b). Compared to the visibility coefficient spectrum, the mean value spectrum $a_0(E)$, shown in Fig. 3 (c) and (d), exhibit greater consistency with changes in divergence angle and inter-grating distance. According to the modeling results, one important implication is that the shape of the visibility spectrum $V_1(E)$ is strongly influenced by the divergence angle and inter-grating distance, which will significantly affect the behavior of the beam-hardening effect, as predicted by Eq. (20).

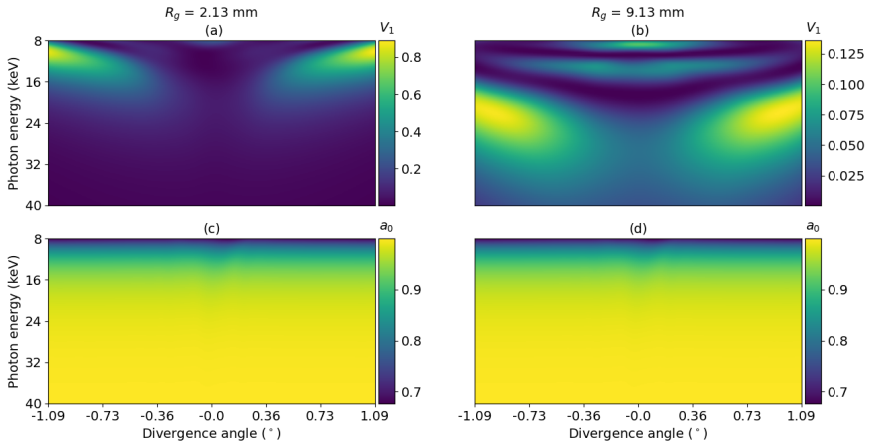

Fig. 3. Spectral properties modeled in the simulation for two inter-grating distances R_g. The left and right columns show the results for the inter-grating distances of 2.13 mm and 9.13 mm, respectively. (a) and (b) illustrate the spatial and energy dependencies of the 1st-order visibility coefficient. The energy dependencies of the visibility coefficient, along the axis of photon energy, change significantly with the divergence angle and the inter-grating distance. (c) and (d) show the results for the mean value a_0. The energy dependencies of the mean value are nearly insensitive to changes in the divergence angle and the inter-grating distance.

Optics EXPRESS

3.3. Attenuation function determination

Besides the spectral properties of the set-up, knowledge of the pixel-wise attenuation function $T^{(i,j)}(E)$ is required as well to estimate the attenuation-based visibility change $\hat{D}_{l,\mathrm{att}}^{(i,j,R_g)}$. As only the spectral-averaged attenuation can be obtained from the set-up, we utilize Eq. (16) to retrieve the attenuation function. In this work, we impose a similar criterion on our samples as given in [39], where the energy dependence of the attenuation is assumed to be uniform and known across all pixels. This criterion is valid for all our single-material samples. Estimating the attenuation function for inhomogeneous samples will be discussed in Section 4.

Based on our criterion and Eq. (16), the expected attenuation contrast is formulated as:

$$\hat{T}^{(i,j)} = \frac{\sum_E S_0(E) \cdot a_0^{(i)}(E) \cdot \exp\left[-\frac{\mu}{\rho}(E) \cdot \rho \cdot d^{(i,j)}\right]}{\sum_E S_0(E) \cdot a_0^{(i)}(E)}, \tag{21}$$

with $\frac{\mu}{\rho}(E)$ the mass attenuation coefficient including total attenuation with coherent scattering, ρ the density, and d the projected thickness of the sample. With the attenuation contrast retrieved from the measurement, denoted as $\overline{T}^{(i,j)}$, the pixel-wise sample thickness can be obtained by minimizing the absolute difference between the measured attenuation $\overline{T}^{(i,j)}$ and the expected attenuation $\hat{T}^{(i,j)}$, given by:

$$d^{(i,j)} = \arg\min|\overline{T}^{(i,j)} - \hat{T}^{(i,j)}|. \tag{22}$$

Once the sample thickness for each pixel is obtained, the attenuation function can be determined accordingly:

$$T^{(i,j)}(E) = \exp\left[-\frac{\mu}{\rho}(E) \cdot \rho \cdot d^{(i,j)}\right]. \tag{23}$$

Six samples with uniform thicknesses were measured, and their material and designed thicknesses are listed in Table 1. Then, based on Eq. (22), the corresponding pixel-wise thicknesses are retrieved through the minimization process, covering a total of 2322×500 pixels. Specifically, we choose to use the Nelder–Mead method with a tolerance of 10^{-6}. The mass attenuation coefficients $\frac{\mu}{\rho}(E)$ are obtained from NIST [46], and the densities ρ are provided by the manufacturers. The retrieved thicknesses display a Gaussian distribution among all pixels and their corresponding mean value and standard deviation are presented in Table 1.

Table 1. The table presents information on the thicknesses of six samples, including the designed thicknesses provided by the manufacturers and the thicknesses retrieved from the optimization procedures. Overall, thicknesses for 2322×500 pixels were retrieved, and their corresponding mean values and standard deviations are listed.

Material	Aluminum	Aluminum	Aluminum	Molybdenum	PMMA	PVC
Designed (μm)	450	750	1000	25	3200	920
Retrieved (μm)	472(±12)	798(±18)	1038(±22)	24(±0.4)	3318(±151)	998(±23)

Although the deviations between the designed and retrieved thicknesses are within acceptable limits, the discrepancies suggest that our model's spectral properties, as represented by $S_0(E)\cdot a_0(E)$, do not fully match the experimental conditions. As seen from Table 1, the retrieved thicknesses of aluminum, PMMA, and PVC are all overestimated. Given that the attenuation coefficients for these three materials monotonically decrease with the photon energy within our energy range, the overestimation of the thicknesses indicates that the simulated average energy of $S_0(E) \cdot a_0(E)$ is lower than the actual value. In contrast, an opposite error was found for molybdenum. This can be consistent with the lower simulated energy due to the presence of the K-edge at 20 keV. With the knowledge of pixel-wise thicknesses, the attenuation functions are constructed based on Eq. (23).

Optics EXPRESS

3.4. Beam hardening correction for dark-field signal

The definition of the dark-field signal in this study is based on the logarithmic change of the visibility coefficient. Thus, the dark-field signal produced by a sample is determined by the measured visibility coefficient change $\overline{D}_l^{(i,j,R_g)}$, given as:

$$DF_l^{(i,j,R_g)} = -\ln \overline{D}_l^{(i,j,R_g)}. \tag{24}$$

In DPGI, the change in visibility coefficient is linked to distinct diffraction orders (l), leading to the definition of the dark-field signal in accordance with the relevant diffraction order. If the concept of the dark-field signal is restricted to describing solely the SAS signals of the sample, all the samples presented in Table 1 should not generate any dark-field signal, since they mainly attenuate the beam with negligible small-angle scattering. However, the beam-hardening effect causes not only the generation of the non-zero dark-field signal by these samples, but also a substantial variation in the dark-field signal with changes in the divergence angle and inter-grating distance. Figure 4 displays a representative example, where the red lines correspond to the dark-field signal (1st diffraction order) obtained from the aluminum foil of 750 µm thickness, at 10 different inter-grating distances. The dark-field signal is averaged along the y-axis across 500 pixels to increase the statistics. As we can see, the magnitudes of the attenuation-based dark-field signal can be significant, and their values can be either positive or negative. Moreover, the experimental results are consistent with the predictions of the modeled spectral properties (see Fig. 3), as the dark-field signal induced by beam hardening also exhibits symmetry around the normal incident angle and is closely related to the divergence angle. Furthermore, with the inter-grating distance R_g adjusted, both the magnitudes and spatial dependencies change greatly. For example, at the inter-grating distance of 2.13 mm , the beam-hardening effect is significant, at wide divergence angles. Moreover, the magnitude of the beam-hardening effect changes fast with the divergence angle. However, when the inter-grating distance is changed to 11.13 mm , the magnitude of beam-hardening induced dark-field signal is lower and more constant. Figure 4 clearly indicates that without removing the beam-hardening effect, it is almost impossible to quantitatively analyze the sub-resolution structural information of samples.

Combining the modeled spectral properties (in Section 3.2) and the retrieved attenuation function (in Section 3.3), the attenuation-based visibility change $\hat{D}_{l,\mathrm{att}}^{(i,j,R_g)}$ can be fully described according to Eq. (20). Thereby, based on Eq. (18), the dark-field signal can be calculated after performing the beam-hardening correction as follows:

$$DF_{l,\mathrm{corr}}^{(i,j,R_g)} = -\ln\left[\frac{\overline{D}_l^{(i,j,R_g)}}{\hat{D}_{l,\mathrm{att}}^{(i,j,R_g)}}\right]. \tag{25}$$

The corresponding corrected results are shown by the blue lines in Figure 4. The correction algorithm is generally effective in eliminating the beam-hardening effect and isolating the dark-field signal that is specifically associated with the small-angle scattering, resulting in close to zero values for the dark-field signal across all divergence angles and inter-grating distances. Although the corrected dark-field signal is not precisely zero, we can attribute these deviations to the inaccuracies in modeling the spectral properties. For instance, the differences between the designed and retrieved thicknesses (as shown in Table 1) indicate that the modeled spectral properties, $S_0(E) \cdot a_0(E)$, are not entirely consistent with the actual energy dependencies. Moreover, the spatial dependency of the visibility coefficient spectrum $V_l^{(i,R_g)}(E)$ is closely related to the precise shape of the grating. Despite attempts to closely approximate the grating's shape (as detailed in Section 6), duplicating the exact shape in simulation remains a challenging or infeasible task.

Optics EXPRESS

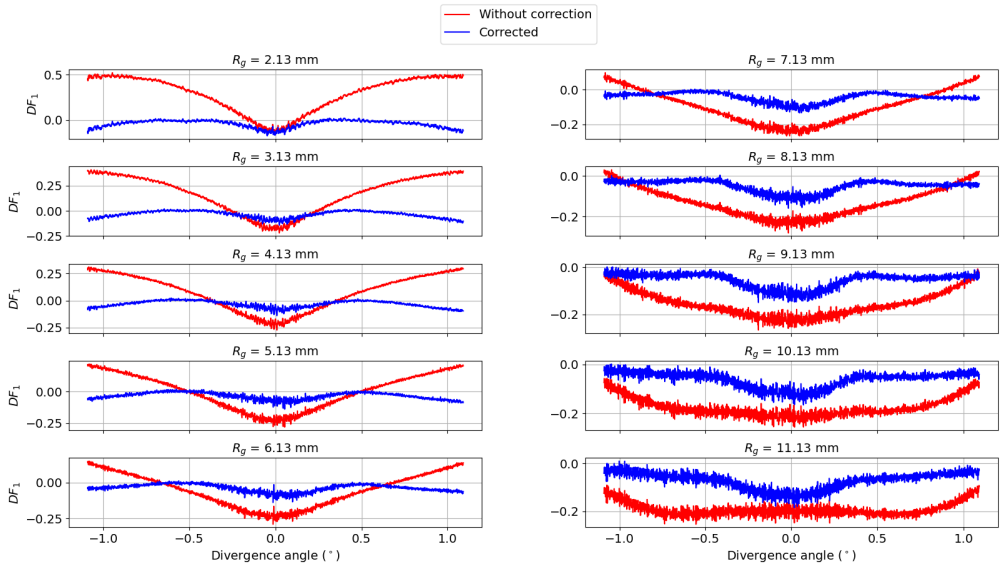

Fig. 4. Comparisons of the 1st-order dark-field signal measured from a 750 µm thick aluminum foil with and without beam-hardening correction. The red lines represent the retrieved dark-field signal averaged along the y-axis for 500 pixels before the correction is applied. The beam-hardening effect varies greatly with the divergence angle and the inter-grating distance R_g. The blue lines are the corrected results. The correction algorithm can effectively eliminate the beam-hardening effect, resulting in the dark-field signal that is close to zero with limited biases.

Besides the aluminum sample with a thickness of 750 µm, the correction results for all six samples are plotted in Fig. 5. Instead of repeating Fig. 4 six times, we choose three representative divergence angles, 0.81, 0.53, and 0.25 degrees, each distinguished by distinct colors, and plot the dark-field signal (1st diffraction order) as a function of the inter-grating distance. The dark-field signal is averaged along the y-axis for 500 pixels, and the corresponding standard deviations are plotted as error bars. The solid lines represent the results without correction, while the non-solid lines present the corresponding corrected dark-field signal. The successful correction of the beam-hardening effect for all samples in Fig. 5 validates the accuracy and robustness of the correction algorithm. While there are small biases in the corrected dark-field signal that deviate from zero, they remain constant across inter-grating distances for a given sample. Moreover, the beam-hardening effect for the molybdenum filter exhibits a different trend compared to the other samples. Due to the presence of a K-edge in its attenuation function, the beam-hardening effect increases with the inter-grating distance rather than decreases.

As shown in the appendix (Fig. 9), the visibility coefficient for the 2nd diffraction order is not negligible when the divergence angle is around zero. In analogy to Fig. 5, Fig. 6 illustrates the beam-hardening correction results for the 2nd diffraction order, when the divergence angle is zero. It is clear that the correction algorithm effectively operates for the first five inter-grating distances, for all samples. However, beyond that point, the corrected dark-field signal is not constant around zero. This is expected since the magnitudes of the 2nd-order visibility coefficient become extremely low when the inter-grating distance exceeds 6.13 mm (see Fig. 9). As a result, the dark-field signal cannot be accurately retrieved. This is reflected by the fast-increasing standard deviations for longer inter-grating distance, as shown in Fig. 6.

Optics EXPRESS

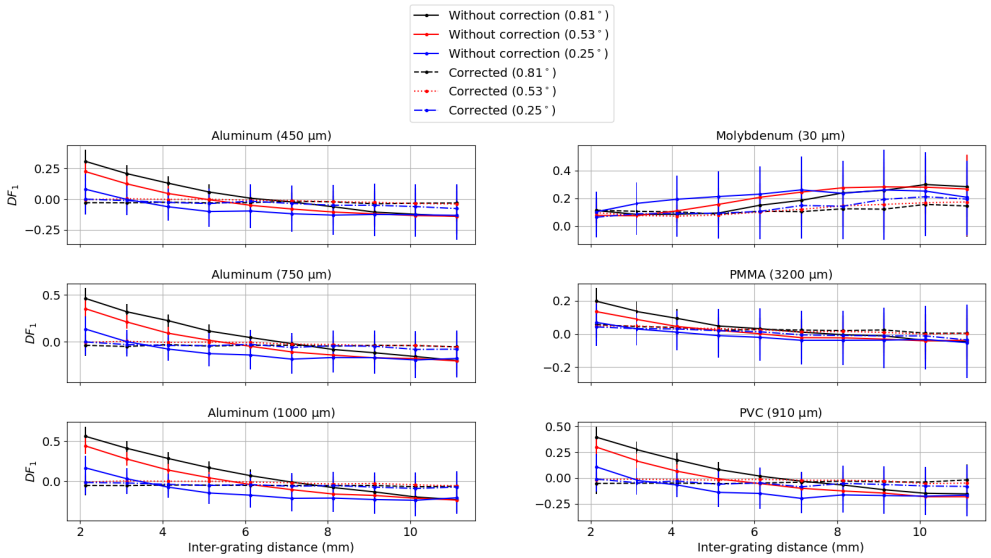

Fig. 5. The figure presents the 1st-order dark-field signal for all six samples, with and without beam-hardening correction. The dark-field signal is plotted as a function of inter-grating distance for three representative divergence angles: 0.81 degrees in black, 0.53 degrees in red, and 0.25 degrees in blue. The solid lines represent the measurement results before correction, while the non-solid lines represent the corrected results. The dark-field signal is averaged along the y-axis and the standard deviations are plotted as error bars. The success of the beam-hardening removal for all samples has been presented, leading to the close-to-zero dark-field signal.

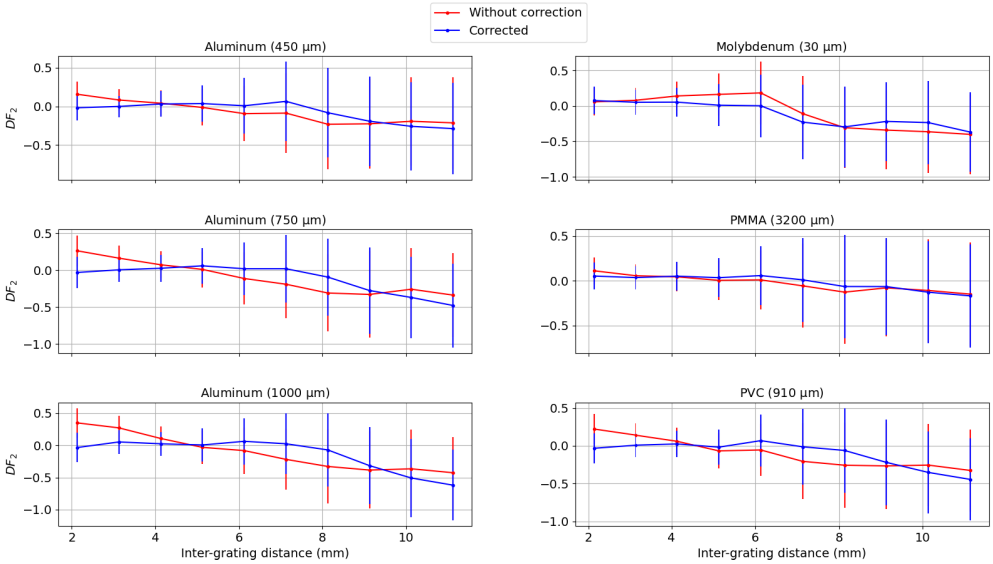

Fig. 6. The figure displays a comparison of the 2nd-order dark-field signal for all six samples, with and without beam-hardening correction, at a divergence angle of zero degrees. The dark-field signal is averaged along the y-axis and the standard deviations are plotted as error bars. The success of the beam-hardening removal for the first five inter-grating distances has been presented, leading to the close-to-zero dark-field signal.

Optics EXPRESS

4. Discussion

As previously discussed, compared to XT-GI, DPGI offers several benefits, including improved dose efficiency by removing the analyzer grating and the ability to adjust the correlation length without altering the sample's magnification. However, DPGI is particularly susceptible to the beam-hardening effect in the dark-field signal. The red lines depicted in Figure 4 illustrate that, even in the absence of small-angle scattering, a pure absorption sample (750 μm aluminum foil) can yield substantial dark-field signal. Moreover, the magnitude of the dark-field signal is highly dependent on the divergence angle and inter-grating distance. If the beam-hardening effect is not corrected, it is not possible to extract accurate small-angle scattering structural information from the relationship between dark-field signal and inter-grating distance. This work introduces a novel beam-hardening correction algorithm, accounting for all the impacts from divergence angle, inter-grating distance, and diffraction order. The effectiveness of the algorithm was verified by the experimental results obtained from six distinct pure absorption samples (see Fig. 4–Fig. 6).

The proposed beam-hardening correction algorithm is based on a simulation model that provides prior knowledge of the spectral properties of the set-up. This feature allows the algorithm to be easily adapted to other measurement settings and set-up geometries, thereby enhancing its versatility and applicability. Nevertheless, the dependence on prior knowledge implies that any discrepancies between the modeled and the actual spectral properties will introduce biases in the corrected results. As shown in Fig. 4, 5 and 6, the corrected dark-field signal is not strictly zero. Although a more accurate estimation of the effective energy and grating shape would enhance the performance of the beam-hardening correction algorithm, our study demonstrates that the algorithm can still effectively and robustly remove the beam-hardening effect even under conditions of some uncertainty. The results presented in this work show the correction to materials that should not generate any scattering-based dark-field signal. Beam hardening correction of different scattering objects has been satisfactorily performed with this algorithm and a manuscript about these results is under peer review. The beam-hardening correction makes it possible to relate some micro-structural information to the dark-field signal.

Two limitations of the current algorithm should be mentioned. Firstly, the energy dependency of the attenuation function in this work is assumed to be uniform across the entire field of view and has been tabulated. However, when samples exhibit non-uniform energy dependency, the optimization process, given by Eq. (22), to find the pixel-wise attenuation function is not valid. To handle these situations, the energy dependencies can be parameterized instead of using a tabulated function, as described in [39,43]. Then, the parameters are determined by fitting the attenuation function to the measured absorption results obtained under different spectra. The second limitation of the current beam-hardening correction algorithm arises in samples that exhibit differential phase contrast, which can further reduce the visibility coefficient due to dispersion in a polychromatic spectrum [41,42]. According to the analytical model derived by De Marco et al. [42] and combining the spectral properties modeled in this work, the visibility reduction due to dispersion can be estimated once the energy-dependent phase shift has been determined. As we know, a number of investigations have been made to extract the energy dependency of phase shift from the samples [33,36,38,39]. Therefore, it is possible to extend the current correction algorithm to eliminate this dispersion effect in the dark-field signal as well.

5. Conclusion

The beam-hardening effect in the dark-field signal makes quantitative sub-resolution structural information inaccessible, and this effect in DPGI varies with the divergence angle, inter-grating distance, and diffraction order. To address this issue, this paper presents a correction algorithm that can effectively remove the beam-hardening effect. The accuracy and robustness of the algorithm are validated by the experimental results for six samples with distinct attenuation

Optics EXPRESS

functions. This algorithm paves the way for quantitatively accessing the small-angle scattering structural information from the relationship between the dark-field signal and the correlation length.

Appendix

In this section, we present the grating shape and unsharpness of the detector used in the simulation. Additionally, we will provide a comparison between the visibility coefficients obtained from the simulation and those obtained experimentally.

Fig. 7(a) shows a cross-sectional image of one grating, obtained from a scanning electron microscope (SEM) with low magnification. The cross section was realized by cleaving the (100) oriented silicon wafer since the lines were patterned along the (110) crystallographic axis. The grating profile suffers from typical etching defects: the tapering of the silicon lamellas is due to the etching of high aspect ratio trenches (56:1), while the scallops in the top part are the typical defects of Bosch process used in deep reactive ion etching. The strengthening of new etching methods will provide in the future sharper silicon profiles at even higher aspect ratio [47].

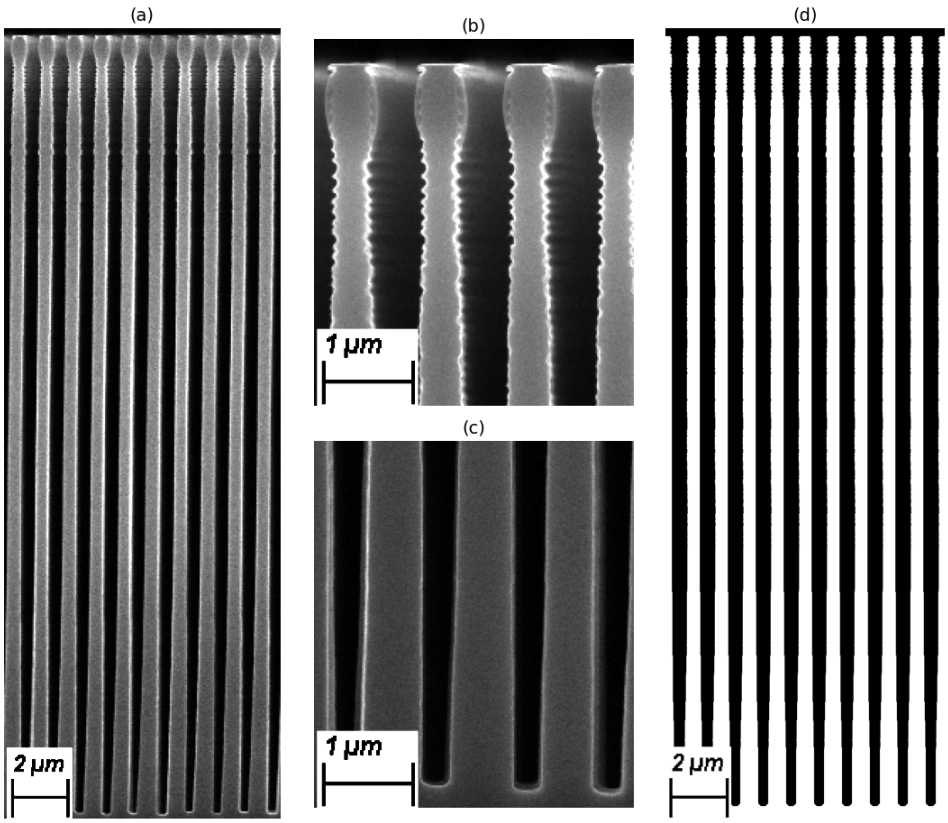

Fig. 7. (a) presents a full cross-sectional profile of the used gratings from a scanning electron microscope (SEM) with low magnification. (b) and (c) show the detailed structural information for the top and bottom parts, respectively, with high magnification. It can be seen from (b) that the tips of the gratings are covered by some polymer residuals of Bosch process used in deep reactive ion etching that are transparent for X-rays. Based on all information from (a) to (c), a typical grating shape is constructed to closely resemble the SEM images, as shown in (d).

Optics EXPRESS

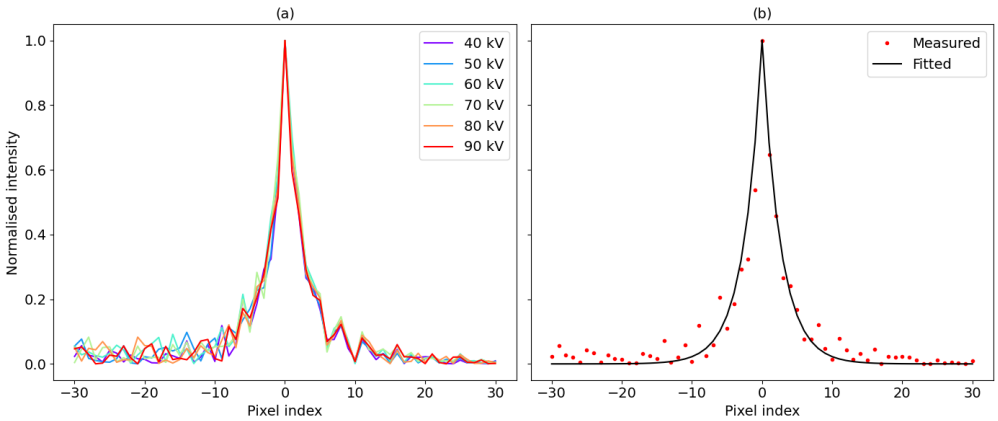

Fig. 8. (a) depicts the measured line spread function (LSF) at different source voltages. The red dots in (b) represent the measured LSF at the source voltage 40 kV, and the black line is the fitted results by a Laplace function.

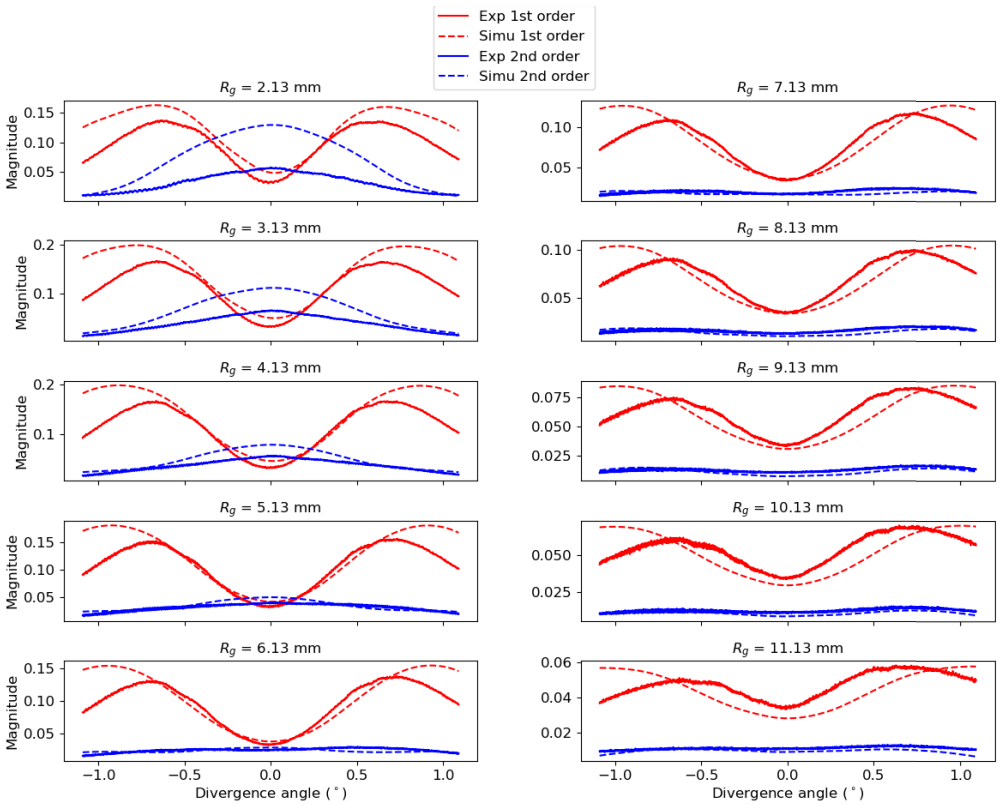

Fig. 9. Comparisons between the experimental (solid) and simulated (dashed) visibility coefficients at 10 different inter-grating distances. The red and blue colors represent 1st and 2nd diffraction orders, respectively.

Fig. 7(b) and (c) show high-magnification images of the top and bottom parts of one grating, respectively, providing detailed views of their structures. Based on the structural information obtained from SEM, the eventual cleaving artifacts have been averaged, and the typical grating

Optics EXPRESS

shape is extracted, as shown in Fig. 7 (d). The white regions in the image represent silicon, while the black regions represent air.

Since DPGI is a technique that directly resolves the interference patterns, the unsharpness from the detector significantly influences the contrast of the fringes. The edge response of the detector was measured by imaging a sharp edge of a 0.09 mm tantalum foil attached to the detector. The resulting edge response was used to calculate the line spread function (LSF) by taking the first derivative [44]. To investigate how photon energy influences the resolving power of the detector, the LSF was extracted at different source voltages, ranging from 40 kV to 90 kV in increments of 10 kV, as plotted in Fig. 8 (a). Our results indicate that the source voltage has a limited effect on the LSF, therefore, LSF can be considered constant across a range of photon energies. According to the shape of the measured LSF, a Laplace distribution was used to fit the measurement results at 40 kV, as depicted in Fig. 8 (b). Then the fitted distribution was used as LSF in the simulation.

Finally, Fig. 9 presents a quantitative comparison between the visibility coefficients obtained from the measurement and the simulation, at 10 different inter-grating distances. The solid lines represent the measured visibility coefficient, which is averaged along the y-axis for 500 pixels, while the corresponding simulated results are plotted as dashed lines. The 1st and 2nd diffraction orders are shown in red and blue, respectively. As shown in Fig. 9, the simulation can correctly model the visibility coefficients, both in terms of spatial dependencies and magnitudes, with tolerable deviations. These deviations are expected due to the imperfect modeling of the actual grating shape, line spread function (LSF), and effective spectrum. As shown in Fig. 9, the visibility coefficients for the 1st diffraction order exhibit symmetric peaks at non-zero divergence angles. Additionally, the visibility coefficients for the 2nd diffraction order are not negligible for the short inter-grating distances.

Funding. Interreg Vlaanderen-Nederland (Smart*Light); European Regional Development Fund (Smart*Light); Provincie Oost-Vlaanderen (Smart*Light); Fonds Wetenschappelijk Onderzoek (3179I12018); Schweizerischer Nationalfonds zur Förderung der Wissenschaftlichen Forschung (CRSII5_183568); Personalized Health and Related Technologies (PHRT) (2022-572).

Acknowledgments. We acknowledge our technicians Sander Vanheule, Yen Decappelle, Iván Josipovic and Patrick Sennesel from the Radiation Physics research group at Ghent University for their technical support. We thank the clean room facilities of PSI, Z. Shi and K. Jefimovs for the gratings etching.

Disclosures. The authors declare no conflicts of interest related to this article.

Data availability. Data underlying the results presented in this paper are not publicly available at this time but may be obtained from the authors upon reasonable request.

References

1. A. Momose, S. Kawamoto, I. Koyama, Y. Hamaishi, K. Takai, and Y. Suzuki, "Demonstration of x-ray talbot interferometry," Jpn. J. Appl. Phys. **42**(Part 2, No. 7B), L866–L868 (2003).
2. A. Momose, "Recent advances in x-ray phase imaging," Jpn. J. Appl. Phys. **44**(9R), 6355–6367 (2005).
3. T. Weitkamp, A. Diaz, C. David, F. Pfeiffer, M. Stampanoni, P. Cloetens, and E. Ziegler, "X-ray phase imaging with a grating interferometer," Opt. Express **13**(16), 6296–6304 (2005).
4. F. Pfeiffer, T. Weitkamp, O. Bunk, and C. David, "Phase retrieval and differential phase-contrast imaging with low-brilliance x-ray sources," Nat. Phys. **2**(4), 258–261 (2006).
5. F. Pfeiffer, O. Bunk, C. Kottler, and C. David, "Tomographic reconstruction of three-dimensional objects from hard x-ray differential phase contrast projection images," Nucl. Instrum. Methods Phys. Res., Sect. A **580**(2), 925–928 (2007).
6. F. Pfeiffer, M. Bech, O. Bunk, P. Kraft, E. F. Eikenberry, C. Brönnimann, C. Grünzweig, and C. David, "Hard-x-ray dark-field imaging using a grating interferometer," Nat. Mater. **7**(2), 134–137 (2008).
7. T. Donath, F. Pfeiffer, O. Bunk, C. Grünzweig, E. Hempel, S. Popescu, P. Vock, and C. David, "Toward clinical x-ray phase-contrast ct: demonstration of enhanced soft-tissue contrast in human specimen," Investig. radiology **45**(7), 445–452 (2010).
8. M. Engelhardt, J. Baumann, M. Schuster, C. Kottler, F. Pfeiffer, O. Bunk, and C. David, "High-resolution differential phase contrast imaging using a magnifying projection geometry with a microfocus x-ray source," Appl. Phys. Lett. **90**(22), 224101 (2007).

Optics EXPRESS

9. P. Zhu, K. Zhang, Z. Wang, Y. Liu, X. Liu, Z. Wu, S. A. McDonald, F. Marone, and M. Stampanoni, "Low-dose, simple, and fast grating-based x-ray phase-contrast imaging," Proc. Natl. Acad. Sci. U.S.A. **107**(31), 13576–13581 (2010).
10. M. Stampanoni, Z. Wang, T. Thüring, *et al.*, "Toward clinical differential phase contrast mammography: preliminary evaluations and image processing schemes," J. Inst. **8**(05), C05009 (2013).
11. H. F. Talbot, "Lxxvi. facts relating to optical science. no. iv," The London, Edinburgh, Dublin Philos. Mag. J. Sci. **9**(56), 401–407 (1836).
12. Z.-T. Wang, K.-J. Kang, Z.-F. Huang, and Z.-Q. Chen, "Quantitative grating-based x-ray dark-field computed tomography," Appl. Phys. Lett. **95**(9), 094105 (2009).
13. M. Bech, O. Bunk, T. Donath, R. Feidenhans, C. David, and F. Pfeiffer, "Quantitative x-ray dark-field computed tomography," Phys. Med. Biol. **55**(18), 5529 (2010).
14. W. Yashiro, Y. Terui, K. Kawabata, and A. Momose, "On the origin of visibility contrast in x-ray talbot interferometry," Opt. Express **18**(16), 16890–16901 (2010).
15. S. K. Lynch, V. Pai, J. Auxier, A. F. Stein, E. E. Bennett, C. K. Kemble, X. Xiao, W.-K. Lee, N. Y. Morgan, and H. H. Wen, "Interpretation of dark-field contrast and particle-size selectivity in grating interferometers," Appl. Opt. **50**(22), 4310–4319 (2011).
16. M. Strobl, "General solution for quantitative dark-field contrast imaging with grating interferometers," Sci. Rep. **4**(1), 7243 (2014).
17. F. Prade, A. Yaroshenko, J. Herzen, and F. Pfeiffer, "Short-range order in mesoscale systems probed by x-ray grating interferometry," Europhys. Lett. **112**(6), 68002 (2015).
18. R. Andersson, L. F. Van Heijkamp, I. M. De Schepper, and W. G. Bouwman, "Analysis of spin-echo small-angle neutron scattering measurements," J. Appl. Crystallogr. **41**(5), 868–885 (2008).
19. L. Feigin and D. I. Svergun, *Structure analysis by small-angle X-ray and neutron scattering*, vol. 1 (Springer, 1987).
20. Z. Shi, K. Jefimovs, L. Romano, and M. Stampanoni, "Towards the fabrication of high-aspect-ratio silicon gratings by deep reactive ion etching," Micromachines **11**(9), 864 (2020).
21. R. P. Harti, M. Strobl, B. Betz, K. Jefimovs, M. Kagias, and C. Grünzweig, "Sub-pixel correlation length neutron imaging: Spatially resolved scattering information of microstructures on a macroscopic scale," Sci. Rep. **7**(1), 44588 (2017).
22. S. Lee, O. Oh, Y. Kim, D. Kim, J. Won, and S. W. Lee, "Study on dark-field imaging with a laboratory x-ray source: Random stress variation analysis based on x-ray grating interferometry," Rev. Sci. Instrum. **92**(1), 015103 (2021).
23. B. K. Blykers, C. Organista, M. N. Boone, M. Kagias, F. Marone, M. Stampanoni, T. Bultreys, V. Cnudde, and J. Aelterman, "Tunable x-ray dark-field imaging for sub-resolution feature size quantification in porous media," Sci. Rep. **11**(1), 18446 (2021).
24. S. Gkoumas, P. Villanueva-Perez, Z. Wang, L. Romano, M. Abis, and M. Stampanoni, "A generalized quantitative interpretation of dark-field contrast for highly concentrated microsphere suspensions," Sci. Rep. **6**(1), 35259 (2016).
25. H. Miao, A. Panna, A. A. Gomella, E. E. Bennett, S. Znati, L. Chen, and H. Wen, "A universal moiré effect and application in x-ray phase-contrast imaging," Nat. Phys. **12**(9), 830–834 (2016).
26. M. Kagias, Z. Wang, K. Jefimovs, and M. Stampanoni, "Dual phase grating interferometer for tunable dark-field sensitivity," Appl. Phys. Lett. **110**(1), 014105 (2017).
27. A. Yan, X. Wu, and H. Liu, "Quantitative theory of x-ray interferometers based on dual phase grating: fringe period and visibility," Opt. Express **26**(18), 23142–23155 (2018).
28. A. Yan, X. Wu, and H. Liu, "Predicting fringe visibility in dual-phase grating interferometry with polychromatic x-ray sources," J. XST **28**(6), 1055–1067 (2020).
29. A. Yan, X. Wu, and H. Liu, "Sample phase gradient and fringe phase shift in dual phase grating x-ray interferometry," Opt. Express **27**(24), 35437–35447 (2019).
30. A. Yan, X. Wu, and H. Liu, "Clarification on generalized lau condition for x-ray interferometers based on dual phase gratings," Opt. Express **27**(16), 22727–22736 (2019).
31. J. Bopp, V. Ludwig, M. Seifert, G. Pelzer, A. Maier, G. Anton, and C. Riess, "Simulation study on x-ray phase contrast imaging with dual-phase gratings," Int. J. CARS **14**(1), 3–10 (2019).
32. Y. Ge, J. Chen, P. Zhu, *et al.*, "Dual phase grating based x-ray differential phase contrast imaging with source grating: theory and validation," Opt. Express **28**(7), 9786–9801 (2020).
33. A. Yan, X. Wu, and H. Liu, "Polychromatic x-ray effects on fringe phase shifts in grating interferometry," Opt. Express **25**(6), 6053–6068 (2017).
34. C. Organista, M. Kagias, R. Tang, Z. Shi, K. Jefimovs, M. N. Boone, and M. Stampanoni, "Optimization of the visibility of a tunable dual-phase x-ray grating interferometer," Opt. Continuum **2**(1), 232–248 (2023).
35. J. M. Cowley, *Diffraction physics* (Elsevier, 1995), pp. 8–11.
36. M. Engelhardt, C. Kottler, O. Bunk, C. David, C. Schroer, J. Baumann, M. Schuster, and F. Pfeiffer, "The fractional talbot effect in differential x-ray phase-contrast imaging for extended and polychromatic x-ray sources," J. Microsc. **232**, 145–157 (2008).
37. M. Chabior, T. Donath, C. David, O. Bunk, M. Schuster, C. Schroer, and F. Pfeiffer, "Beam hardening effects in grating-based x-ray phase-contrast imaging," Med. Phys. **38**(3), 1189–1195 (2011).
38. P. R. Munro and A. Olivo, "X-ray phase-contrast imaging with polychromatic sources and the concept of effective energy," Phys. Rev. A **87**(5), 053838 (2013).

Optics EXPRESS

39. A. Yan, X. Wu, and H. Liu, "Beam hardening correction in polychromatic x-ray grating interferometry," Opt. Express **25**(20), 24690–24704 (2017).
40. W. Yashiro, P. Vagovič, and A. Momose, "Effect of beam hardening on a visibility-contrast image obtained by x-ray grating interferometry," Opt. Express **23**(18), 23462–23471 (2015).
41. G. Pelzer, G. Anton, F. Horn, J. Rieger, A. Ritter, J. Wandner, T. Weber, and T. Michel, "A beam hardening and dispersion correction for x-ray dark-field radiography," Med. Phys. **43**(6Part1), 2774–2779 (2016).
42. F. De Marco, J. Andrejewski, K. Willer, L. Gromann, T. Koehler, H.-I. Maack, J. Herzen, and F. Pfeiffer, "X-ray dark-field signal reduction due to hardening of the visibility spectrum," arXiv, arXiv:2011.03542 (2020).10.48550/arXiv.2011.03542
43. A. Pandeshwar, M. Kagias, Z. Wang, and M. Stampanoni, "Modeling of beam hardening effects in a dual-phase x-ray grating interferometer for quantitative dark-field imaging," Opt. Express **28**(13), 19187–19204 (2020).
44. R. Tang, C. Organista, W. Goethals, W. Stolp, M. Stampanoni, J. Aelterman, and M. N. Boone, "Detailed analysis of the interference patterns measured in lab-based x-ray dual-phase grating interferometry through wave propagation simulation," Opt. Express **31**(2), 1677–1691 (2023).
45. J. Dhaene, "Development and application of a highly accurate polychromatic x-ray microtomography simulator," Ph.D. thesis, Ghent University (2017).
46. J. Hubbell, "Tables of x-ray mass attenuation coefficients and mass energy-absorption coefficients (version 1.4)," http://physics.nist.gov/xaamdi (2004).
47. Z. Shi, K. Jefimovs, M. Stampanoni, and L. Romano, "High aspect ratio arrays of si nano-pillars using displacement talbot lithography and gas-macetch," Mater. Sci. Semicond. Process. **157**, 107311 (2023).